PAPER

Check for updates

Cross-correlated experimental and theoretical characterisation of orpiment As$_2$S$_3$, a potential material for new advanced technological applications†

Gianfranco Ulian, [iD] Francesca Ranellucci and Giovanni Valdrè [iD] *

In the ever-growing search for new materials in optical, electronic and photovoltaic applications, chalcogenides, such as amorphous diarsenic trisulfide (As$_2$S$_3$), are being deeply investigated. However, very few and incomplete data are available on crystalline As$_2$S$_3$ (space group $P2_1/n$), known as mineral orpiment. In the present work, several experimental techniques were employed to analyse the crystal structure, morphology, chemical composition and vibrational properties of the bulk and mechanically cleaved (010) orpiment surface. Also, cross-correlated atomic-scale *ab initio* simulations corroborated and explained the new experimental data. Orpiment showed a semiconducting behaviour, with an indirect band gap of 2.44 eV and an optical Γ–Γ gap of 2.63 eV, which agrees with previous optical-absorption edge measurements. Furthermore, the complete stiffness tensor and the phonon band structure were reported for the first time. All these quantities are of utmost importance for devising new possible applications of crystalline orpiment in the technological and materials science fields.

Introduction

In the last decades, the world population has exponentially increased its energy requirements for daily, industrial, and third-sector activities. On the one hand, this need is translated into an increase in the consumption of fossil fuels (carbon, oil) and other non-renewable resources, a trend that rose by about 51% from 1995 to 2015 and it is expected to increase by another 18% from 2015 to 2035.[1] On the other hand, new materials are required for advanced applications in different and manifold fields, *e.g.*, optoelectronics and sensors, efficient conversion of heat electricity (thermoelectric materials), photovoltaic and other renewable energy production systems, catalysis, wearable electronic devices, *etc.*[2–6]

In this context, metal chalcogenide minerals and materials made of sulphur, selenium, and tellurium have gathered significant attention due to their unique properties and versatility in these technological applications and research fields.[7] Among them, diarsenic trisulfide (As$_2$S$_3$) is an interesting material because of its reversible and/or irreversible changes of physico-chemical properties induced by irradiation with light of

suitable energy and intensity or by thermal-annealing, which are peculiar features that can be exploited in optics and optoelectronics.[8] However, most of the research on this material was principally focused on the electronic properties of amorphous glass and thin films,[9] where the physics governing them is related to short-range atomic order. Presently, little information is available on As$_2$S$_3$ crystalline compounds, which instead present periodic structures with long-range order.

The natural equivalent of crystalline As$_2$S$_3$ is known as the mineral orpiment (space group $P2_1/n$, monoclinic crystal system), formed as a hot-spring deposit, an alteration product (especially from realgar), or as a low-temperature product in hydrothermal veins, whose crystallographic features were described in detail in the review of Bonazzi and Bindi.[10] Very briefly, the structure is made of AsS$_3$ pyramids connected *via* S atoms to form diarsenic trisulphide layers (see Fig. 1) stacked along the [010] direction and held by weak (van der Waals) interactions. Differently from those found in other minerals and materials such as graphite, molybdenite MoS$_2$ and phyllosilicates, these layers are not atomic-flat and present a puckered morphology at the sub-nanometric level. However, orpiment shares with the cited compounds the perfect and easy cleavage characteristics of the As$_2$S$_3$ layers [on the (010) plane], thus making this mineral suitable for 2D applications.[11]
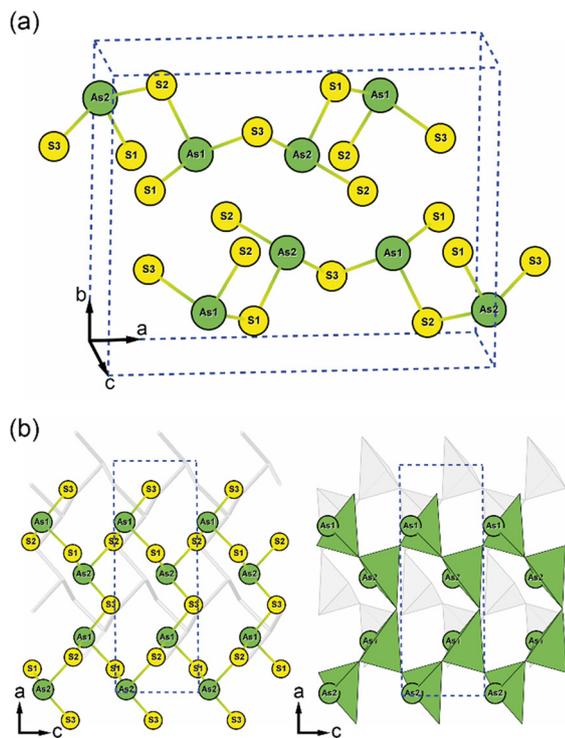
In addition to its technological applications, orpiment was widely used in ancient times as a natural pigment due

Dipartimento di Scienze Biologiche, Geologiche e Ambientali, Università di Bologna, P. Porta San Donato 1, I-40126, Bologna, Italy.
E-mail: giovanni.valdre@unibo.it

Fig. 1 Crystal structure of orpiment. (a) Ball-and-stick representation of the unit cell of orpiment As_2S_3, where the blue dashed lines indicate the unit cell. (b) Structure of a single layer of diarsenic trisulphide as seen from the [010] direction in the crystallographic unit cell, with a ball-and-stick model (on the left) and an As_2S_3 polyhedral representation (on the right). For the sake of clarity, in panel (b) only a single As_2S_3 layer in the unit cell is shown with full opacity to better elucidate its structure.

to its yellow colour, hence its Latin name *auripigmentum* (golden pigment). Archaeometric analyses revealed its presence in several works of art, *e.g.*, in *The Jewish Bride* of Rembrandt[12] and a Viking Age structure in the Surtshellir cave (Iceland).[13]

For the identification of orpiment in cultural heritage, destructive and non-invasive techniques such as X-ray fluorescence and Raman spectroscopy are employed. However, concerning the latter technique, very few studies in the scientific literature reported a detailed analysis of crystalline As_2S_3,[14] where not every vibrational band was assigned to specific normal modes. Moreover, confocal Raman spectroscopy is currently used in 2D materials research, *e.g.*, to measure the number of layers in 2D materials by analysing the position, width, and intensity of Raman peaks,[15] to probe the electronic properties and perform qualitative structural characterisation,[16] and to detect strain and thermal conductivity changes.[17] Hence, a detailed knowledge of the vibrational properties of orpiment is required not only for better identification of the mineral for cultural heritage but also for high-quality characterisation of bulk and 2D As_2S_3, to understand its stability and, eventually, to develop new applications and two-dimensional materials such as heterojunctions.

In addition, in the literature there are incomplete data concerning the elastic behaviour of orpiment, where only ten of the thirteen independent elastic stiffness tensor components were obtained by Brillouin scattering experiments.[18] This is an important information regarding the stability of the mineral in both geological/geophysical and materials science/technological fields, which may help the development of new applications of crystalline As_2S_3 in optical and electronic devices.

The present work was conceived to fill the knowledge gaps previously introduced and, at the same time, to provide new insights into the properties of this peculiar mineral, which is a potential material also for 2D applications. To this aim, a cross-correlated experimental and theoretical characterisation of crystalline As_2S_3 extracted from a natural sample was devised. From the experiments, the crystallographic features, chemical composition and Raman spectrum of the bulk, and the morphology and Raman spectra of exfoliated (few-layers) specimens on the (010) crystalline plane were investigated. These new data were corroborated by atomic-scale simulations within the density functional theory (DFT) framework, employing a state-of-the-art computational approach based on the use of hybrid functionals. The cross-correlation of the experimental and theoretical results was used to assess the quality of the simulations, providing consistent and predictive data on the electronic, vibrational and elastic properties of orpiment.

Materials and methods

Orpiment sample and experimental methods

The As_2S_3 orpiment sample used for the present study was a polycrystalline specimen kindly provided by the "G. Bombicci" Mineralogy Museum of the University of Bologna, Italy. This sample can be considered a model system for orpiment because of its purity, and it was then suitable to assess the quality of theoretical simulations. A portion of the mineral was ground to a fine powder before the subsequent analyses. At the same time, orpiment flakes from several nanometres up to a few micrometres thick were carefully separated by mechanical means[19] and deposited on aluminium stubs.

X-ray powder diffraction

X-ray powder diffraction (XRPD) patterns were collected using a Philips PW 1710 diffractometer equipped with a graphite monochromator on the diffracted beam. Cu Kα X-rays were generated with 40 kV and 30 mA power supply. The patterns were collected between 3° and 70° 2θ, with an angular step of 0.02° and an integration time of 2 seconds. The specimen was ground for 20 minutes in an agate mortar and the powder was collected in a lateral-loading holder to avoid or minimize any possible preferential orientation of the crystallites. The diffractograms were analysed with the computer program Profex,[20] which interfaces the BGMN program[21] and was used for the Rietveld refinement within the fundamental parameters approach. The unit-cell

parameters and experimental details of the refinement protocol and results are reported in Table 1.

Environmental scanning electron microscopy

A Thermo Scientific Quattro S environmental scanning electron microscope (ESEM) with a field-emission gun, equipped with backscattered electron (BS) and cathodoluminescence (CL) detectors and X-ray microanalysis with a silicon-drift detector (SDD-EDS), was employed to study the morphology and local chemistry of the orpiment sample. After careful calibration, the ESEM analyses were carried out under low vacuum conditions, with a water vapour pressure of 100 Pa inside the instrument chamber, an acceleration voltage of 15 kV and a beam current of 0.43 nA. Within these instrumental settings, no conductive coating was needed, obtaining an adequate compromise between imaging resolution and EDS chemical sensitivity.

Confocal Raman microspectrometry

The Raman spectroscopy analysis was performed with a WITec alpha300R confocal Raman microscopy system, made of an optical microscope and an ultra-high throughput UHTS 300 VIS spectrometer with a CCD camera and gratings of 600 g mm^{-1}. Green (532 nm) and red (785 nm) laser beam sources were used for the Raman excitation, setting the power between 1 mW (green laser) and 30 mW (red laser) to prevent heating the sample and photobleaching. The laser beam was focused on the sample with 20×, 50× and 100× Zeiss microscope objectives with a low numerical aperture objective (NA = 0.40) to avoid optical artefacts. The backscattered Raman spectra were collected in confocal mode between 100 and 1700 cm^{-1}, with a resolution of about

Table 1 Crystal data, experimental setup and refinement results of the studied orpiment sample

Parameter	Value
Empirical formula	As_2S_3
Formula weight	246.02
Temperature	298 K
Wavelength	1.540598 Å
Crystal system	Monoclinic
Space group	$P2_1/n$
Unit cell dimensions	$a = 11.42632(8)$ Å
	$b = 9.58649(5)$ Å
	$c = 4.25947(4)$ Å
	$\alpha = \gamma = 90°, \beta = 90.377(6)°$
Unit cell volume	466.570(41) Å^3
Z	4
Density (calculated)	3.502 g cm^{-3}
θ range for data collection	3.0–70.0°
Index ranges	$-8 \leq h \leq 8; -7 \leq k \leq 7; -3 \leq l \leq 3$
No. of points	3351
No. of peaks	402
No. of parameters	63
Refinement method	BGMN
R_{wp}	11.22
R_{exp}	10.39
Goodness-of-fit on F^2	1.08
χ^2	1.17

2.7 cm^{-1} and an acquisition time of 10 minutes. The Rayleigh scattering line was removed using an edge filter.

Computational methods

The simulations reported in the present work were performed using the CRYSTAL17 *ab initio* code, which implements the Kohn–Sham self-consistent field (SCF) method.[22] In the following, details on the computational approach are explained.

Hamiltonian, basis set and computational parameters

Among the several available density functional theory functionals, two hybrid ones were employed, *i.e.*, B3LYP[23,24] and HSE06.[25] The first one is a global hybrid (GH) functional that calculates the total exchange–correlation energy according to the following formula:

$$E_{xc}^{GH} = (1 - A)E_x^{DF} + AE_x^{HF} + E_c^{DF} \tag{1}$$

where E_{xc}, E_x and E_c are the exchange–correlation, exchange and correlation energy terms, respectively, A is the fraction of the exact Hartree–Fock (HF) exchange that is mixed to the density[26] functional (DF) one. In B3LYP, $A = 20\%$, and it also includes a small non-local contribution to both the exchange and correlation contributions to the total energy.

HSE06 is instead a range-separated hybrid (RSH) functional, where the amount of the exact Hartree–Fock exchange depends on the distance between electrons. Currently, three ranges are considered (short, medium, and long) in the separation of the Coulomb operator, according to the following error function:

$$\frac{1}{r_{12}} = \frac{\text{erfc}(\omega_{SR}r_{12})}{r_{12}} + \frac{1 - \text{erfc}(\omega_{SR}r_{12}) - \text{erf}(\omega_{LR}r_{12})}{r_{12}} + \frac{\text{erf}(\omega_{LR}r_{12})}{r_{12}} \tag{2}$$

where the first addendum is the short-range (SR) term, the second one is the middle-range (MR) term and the last one is the long-range (LR) term, and ω is the length scale of separation. Thus, the expression of the exchange–correlation energy for the RSH functional is:

$$E_{xc}^{RSH} = E_{xc}^{DF} + c_{SR}(E_{x.SR}^{HF} - E_{x.SR}^{DF}) + c_{MR}(E_{x.MR}^{HF} - E_{x.MR}^{DF}) + c_{LR}(E_{x.LR}^{HF} - E_{x.LR}^{DF}) \tag{3}$$

where the values of the parameters c and ω define the RSH functional being short-, middle- or long-range corrected. HSE06 is a short-range RSH functional that uses PBE for both the exchange and correlation energies,[27] $A = 25\%$ of the exact Hartree–Fock exchange, and the separation parameters $c_{SR} = 0.25$, $c_{MR} = c_{LR} = 0.00$, and $\omega_{SR} = 0.11$.[25]

Both functionals are well-known in the scientific community for their accuracy in the calculation of the structural,[28,29] vibrational,[30,31] electronic,[32] elastic,[33,34] surface,[35–37] and thermodynamic[38–40] properties. In the

present work, both hybrid functionals were employed, with B3LYP being used mainly to calculate the phonon properties (*e.g.*, IR and Raman spectra) of orpiment, whereas HSE06 was chosen to calculate the electronic band structure of the mineral and monolayers. Geometry optimization of the different models was always carried out with the two functionals before calculating any of the cited properties to ensure the consistency of the data.

However, hybrid DFT functionals do not generally treat long-range interactions accurately, which are fundamental for minerals like orpiment because they hold the As_2S_3 layers together along the *b*-axis direction. In the present work, the DFT-D3 correction was adopted to add *a posteriori* the following contribution to the total energy of the system:[41]

$$E_{\text{DFT-D3}} = -\frac{1}{2} \sum_{i=1}^{N} \sum_{j=1}^{N} \sum_{\mathbf{g}} \left[\begin{array}{c} \frac{C_{6ij}}{r_{ij,\mathbf{g}}^6} f_{\text{dump},6}\left(r_{ij,\mathbf{g}}\right) + \\ \frac{C_{8ij}}{r_{ij,\mathbf{g}}^8} f_{\text{dump},8}\left(r_{ij,\mathbf{g}}\right) \end{array} \right] \quad (4)$$

The sums in eqn (4) are over the atoms N in the unit cell, with $r_{ij,\mathbf{g}}$ being the internuclear distance between atom i in cell $\mathbf{g} = 0$ (reference cell) and atom j in cell $\mathbf{g}$, and C_{nij} ($n = 6$, 8) being the 6th- and 8th-order dispersion coefficients for atom pairs ij. The long-range energy is damped by the functions $f_{\text{dump},6}(r_{ij,\mathbf{g}})$ and $f_{\text{dump},8}(r_{ij,\mathbf{g}})$, to ensure that weak van der Waals interactions do not contribute to other ionic and covalent bonds, which exert their effects at short distances. The damping function $f_{\text{dump},6}(r_{ij,\mathbf{g}})$ is expressed as:

$$f_{\text{dump},6}(r_{ij,\mathbf{g}}) = s_6 \left[1 + e^{-d(r_{ij,\mathbf{g}}/R_{\text{vdW}}-1)} \right]^{-1} \quad (5)$$

with s_6 being a scaling parameter that varies according to the adopted functional (*e.g.*, for PBE it is 0.75), R_{vdW} the sum of van der Waals radii of atoms i and j, and d the steepness of the damping, which was set to 20 in the present work, in agreement with the standard parametrization of the DFT-D2 approach.[42] The $f_{\text{dump},8}(r_{ij,\mathbf{g}})$ is the one proposed by Becke and Johnson,[43–45] which has the following form:

$$f_{\text{dump},6}\left(r_{ij,\mathbf{g}}\right) = \frac{s_n r_{ij}^n}{r_{ij}^n + f\left(R_{0ij}\right)^n} \quad (6)$$

with $R_{0ij} = \sqrt{C_{8ij}/C_{6ij}}$ and $f(R_{0ij}) = \alpha_1 R_{0ij} + \alpha_2$, $s_6 = 1$, $s_8 = 1.9889$, whereas α_1 and α_2 are adjustable parameters. This approach was proved suitable for different kinds of crystalline materials with heterodesmic structures, such as phyllosilicates,[46] layered hydroxides,[47] and composite 2D materials.[32,48] Also, compared to previous formulations, such as the DFT-D2 scheme, the DFT-D3 approach is less empirical.

In CRYSTAL17, the multi-electronic wave function was built from a linear combination of Gaussian-type functions (GTF), within the so-called linear combination of atomic orbitals (LCAO) approach. The arsenic atom was described using a double-zeta molecular basis set that (i) included small-core relativistic effective core potential to treat the relativistic effect of core electrons and (ii) was modified to

reduce too diffuse functions that would lead to numerical instabilities, as described and developed by Heyd *et al.*[49] The sulphur atom was modelled from a modified 6-311G(d) molecular basis set of double-zeta quality used by the same cited authors. Each basis set includes s, p, and d orbitals. Detailed and specific information can be found in the work of Heyd and colleagues.[49]

The total energy was calculated on a pruned grid with 75 radial points and a maximum number of 974 angular points in regions relevant for chemical bonding, subdivided in five shells with different angular grids.[22] The self-consistent field (SCF) iteration was stopped when the energy difference between two consecutive steps was lower than 10^{-8} Ha, whereas a tighter criterion (10^{-10} Ha) was employed for the calculation of the vibrational properties. The numerical accuracy for the calculation of the Coulomb integrals was set to 10^{-7} (ITOL1 to ITOL3 keywords in CRYSTAL), whereas ITOL4 and ITOL5 were set to 10^{-9} and 10^{-30}, respectively. The Hamiltonian matrix was diagonalized on a $6 \times 6 \times 6$ grid[50] with 80k points in the reciprocal space.

Structural relaxation and vibrational properties

The unit cell parameters and atomic coordinates were relaxed at 0 K and 0 GPa using the analytical gradient method for the atomic positions and a numerical gradient for the cell parameters. The Hessian matrix is upgraded with the Broyden–Fletcher–Goldfarb–Shanno algorithm.[51–55] The tolerances for the maximum allowed gradient and the maximum atomic displacement have been set to 10^{-5} Ha bohr^{-1} and 4×10^{-5} bohr, respectively.

Zone-central (*i.e.*, Γ-point) normal modes were calculated by diagonalizing the mass-weighted Hessian matrix W (dynamical matrix), whose elements are the second derivatives of the lattice potential for mass-weighted atomic displacements:[30]

$$W_{\alpha i,\beta j}(\Gamma) = \frac{H_{\alpha i,\beta j}}{\sqrt{M_\alpha M_\beta}} \quad (7)$$

with $H_{\alpha i,\beta j}$ being the energy second derivative, M_α and M_β the atomic masses, and the subscripts in Latin (i, j) and in Greek letters (α, β) the atomic coordinates and the atoms, respectively.

The infrared spectrum was calculated analytically as a raw superposition of p Lorentzian functions, according to the formula:

$$A(v) = \sum_p \frac{I_p}{\pi} \frac{\gamma_p/2}{\left(v - v_p\right)^2 + \gamma_p^2/4} \quad (8)$$

where $A(v)$ is the infrared absorbance, and v_p, γ_p and I_p are the vibrational frequency, the damping factor and the integrated intensity of the pth vibrational mode. The integrated intensity for each mode is given by:

$$I_p = \frac{\pi}{3} \frac{N_A}{c^2} d_p \left| \overrightarrow{Z_p} \right|^2, \quad (9)$$

with N_A being Avogadro's number, c the speed of light, d_p the

degeneracy of the mode and $\overrightarrow{Z_p}$ the mass-weighted effective mode Born charge vector. The latter was obtained analytically through a coupled-perturbed Kohn–Sham (CPKS) approach.[56]

The Raman intensities were calculated using the approximation proposed by Placzek[57] which considers the material as a polycrystalline powder. The intensity was then modelled with a pseudo-Voigt functional form:[58]

$$A(v) = \eta L(v) + (1 - \eta)G(v) \qquad (10)$$

where $A(v)$ represents the Raman intensity and $L(v)$ and $G(v)$ are given by:

$$L(v) = \sum_p \frac{I_p}{\pi} \frac{\varphi_p/2}{(v - v_p)^2 + (\varphi_p/2)^2}, \qquad (11)$$

with I_p being the computed Raman intensity, φ_p the full width at half maximum for the pth vibrational mode, and η the Lorentz factor. The typical sharp bands of Raman spectra were simulated using a pure Lorentzian form ($\eta = 1$). The Raman intensity of the pth mode was calculated according to the following formula:

$$I_p \propto C \left(\frac{\alpha}{\partial Q_p}\right)^2, \qquad (12)$$

where α is the polarizability, and Q_p is the normal mode coordinate for mode p. C is a prefactor that depends on the (angular) frequency of the exciting laser ω_L and the temperature T according to:

$$C \approx (\omega_L - \omega_p)^4 \frac{1}{30\omega_p} \left[1 - e^{-(\hbar\omega_p/k_BT)}\right]^{-1} \qquad (13)$$

with k_B being Boltzmann's constant and ω_p the angular frequency of mode p. In the simulations, the prefactor was calculated setting $T = 298$ K and $\omega_L = 532$ nm to mimic possible experimental conditions. All the tensorial properties related to the intensity of the bands in the infrared and Raman spectra, i.e., the dielectric tensor, and the polarizability, were analytically calculated using a coupled-perturbed Kohn–Sham (CPKS) approach.[59–61]

In addition, phonon dispersion relations were calculated using a supercell approach, considering a $2 \times 2 \times 2$ expansion of the cell (160 atoms), sampling the reciprocal space 8k points.[62]

Calculation of the elastic moduli

The elastic moduli (also known as the stiffness tensor) were calculated using a procedure implemented in the CRYSTAL code,[63] whose formulation and algorithms are briefly explained in this section. Considering an elastic regime of deformation, solids can be described by Hooke's law:

$$\sigma_{ij} = \sum_{kl} C_{ijkl}\varepsilon_{kl} \qquad (14)$$

where i, j, k, and l = 1, 2, 3, σ_{ij} is the stress, ε_{kl} is the strain, and C_{ijkl} are the components of the second-order elastic moduli tensor.[64] The method here adopted to calculate their values uses stress–strain relationships based on total energy calculations, using the following Taylor expansion in terms of the strain components:

$$E(V, \varepsilon) = E(V_0) + V \sum_\alpha \sigma_\alpha\varepsilon_\alpha + \frac{V}{2}\sum_{\alpha\beta} C_{\alpha\beta}\varepsilon_\alpha\varepsilon_\beta + \cdots \qquad (15)$$

In eqn (15), the summation is truncated to the second order and Voigt's notation[64] was used, i.e., α and β = 1, 2, …, 6. V_0 represents the equilibrium volume. The first two terms of eqn (27) are the energy at equilibrium, $E(V_0)$, and the energy related to a strain (ε_α) that is not volume-preserving. The crystalline structure of the solid is assumed to be initially free from stress so that the linear term on the right-hand side in eqn (15) is zero. According to eqn (14), the elastic moduli are then associated with the second derivatives of the total energy with respect to the strain:

$$C_{\alpha\beta} = \frac{1}{V}\frac{\partial^2 E}{\partial\varepsilon_\alpha\partial\varepsilon_\beta}|_0, \qquad (16)$$

where the zero indicates the equilibrium geometry. To include the nuclear relaxation term in eqn (16), the strategy described by Erba[65] was adopted, which evaluates the "internal-strain" tensor of energy second-derivatives for atomic displacements and lattice deformations, as combined with the interatomic force constant Hessian matrix. With this approach, the calculation of the nuclear relaxation is more analytical and computationally robust than previous implementations that relied on relaxing the internal coordinates of the unit cell during deformations.[28,47,66] The analysis of the stiffness tensor was performed using the Quantas code.[67–69]

Results

Crystallography and crystal-chemistry of bulk orpiment

Combined X-ray diffraction and electron microscopy with energy-dispersive spectroscopy were employed to both characterise and provide evidence of the purity of the orpiment specimen. The XRD diffractogram of the powdered
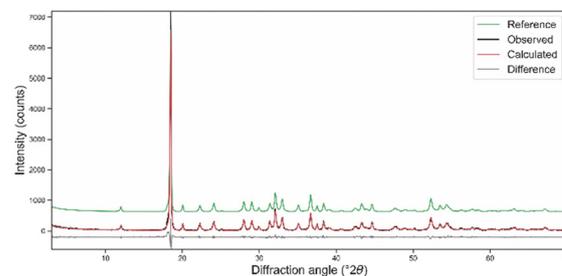
Fig. 2 Powder diffraction data of orpiment As_2S_3 and Rietveld refinement analysis. The difference between the calculated and measured intensities is reported below the profile. The reference XRPD pattern was taken from the American Mineralogist Crystal Structure Database #0010733, related to the sc-XRD data of Mullen and Nowacki.[26]

CrystEngComm

Paper

mineral sample in Fig. 2 presented only the reflections of As_2S_3, with no other minerals within the instrumental sensitivity. The peaks are generally sharp, particularly the one at 18.47° 2θ, highlighting the high crystallinity of the sample.

At the same time, several flakes of the mineral were imaged using environmental scanning electron microscopy and chemically analysed using EDS spectroscopy. An example of one of the orpiment crystalline flakes studied in the present work is shown in Fig. 3a. The flake is large (3.3 mm × 1.4 mm) and presents micrometre-wide atomic-flat areas locally interrupted by folding of the layers (see Fig. 3b–d). In addition, smaller platelets with different thicknesses and pseudo-hexagonal morphologies due to the {100} and {101} forms were observed (Fig. 3b). The flat terraces in the different investigated samples were employed for microchemical analyses with EDS spectroscopy, providing a homogeneous mean atomic composition ($As_{2.05}S_{2.95}$) that is consistent with the ideal orpiment. Examples of the characteristic EDS spectra are reported in Fig. S1 in the ESI.†

From the crystallographic perspective, the Rietveld structural refinement (Table 1) resulted in unit cell parameters a = 11.42632(8) Å, b = 9.58649(5) Å, c = 4.25947(4) Å and β = 90.377(6)°, and the As–S bond lengths were within 2.211 Å and 2.328 Å. The lattice data and internal geometry (bond lengths and angles) are reported in Table 2, whereas the coordinates of the symmetrically inequivalent As and S atoms are presented in Table 3.

The refined orpiment structure was used as the starting model for atomic-scale DFT simulations using the B3LYP-D3 and HSE06-D3 approaches. After relaxing the orpiment lattice and atomic positions within the $P2_1/n$ space group under static conditions (0 K without any vibrational contribution), the calculated crystal volume was smaller than the experimental

Table 2 Crystal structure (lattice parameters and internal geometry) of orpiment As_2S_3 (s.g. $P2_1/n$)

	B3LYP-D3[a]	HSE06-D3[a]	XRPD[a]	sc-XRD[b]
a (Å)	11.626	11.479	11.42632(8)	11.475
b (Å)	9.318	9.221	9.58649(5)	9.577
c (Å)	4.148	4.074	4.25947(4)	4.256
β (°)	90.46	90.55	90.371(6)	90.68
Ω (Å³)	449.355	431.174	466.570(41)	467.685
ρ (g cm⁻³)	3.633	3.786	3.502	3.494
I (Å)	2.015	2.004	2.196	2.146

Bond lengths (Å)

	B3LYP-D3[a]	HSE06-D3[a]	XRPD[a]	sc-XRD[b]
As1–S1	2.293	2.276	2.228	2.292
As1–S2	2.310	2.288	2.315	2.270
As1–S3	2.330	2.308	2.328	2.289
⟨As1–S⟩	2.311	2.291	2.290	2.284
As2–S1	2.328	2.307	2.211	2.308
As2–S2	2.319	2.305	2.211	2.293
As2–S3	2.276	2.254	2.306	2.243
⟨As2–S⟩	2.307	2.288	2.243	2.281

Bond angles (°)

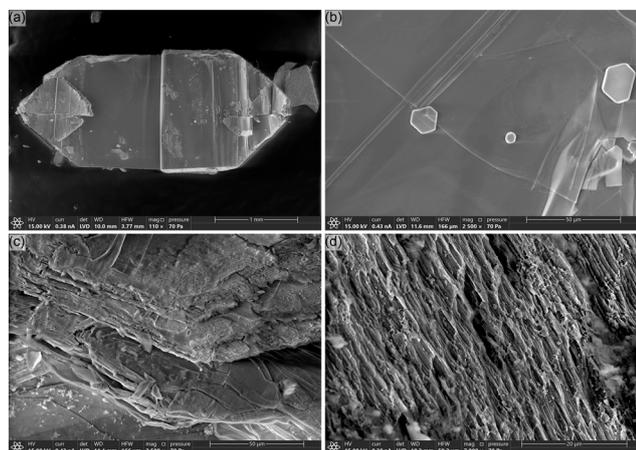|	B3LYP-D3[a]	HSE06-D3[a]	XRPD[a]	sc-XRD[b]
S1–As1–S2	97.90	97.48	97.49	98.61
S1–As1–S3	104.04	103.80	104.58	104.08
S2–As1–S3	93.57	92.99	96.54	94.58
S1–As2–S2	96.94	96.51	99.78	98.61
S1–As2–S3	92.77	91.91	93.52	92.76
S2–As2–S3	105.07	104.62	103.93	104.99
⟨S–As–S⟩	98.38	97.89	99.31	98.94
As1–S1–As2	102.76	102.41	105.63	103.73
As1–S2–As2	100.02	99.53	102.47	100.99
As1–S3–As2	87.18	86.34	86.50	87.94
⟨As–S–As⟩	96.65	96.09	98.20	97.55

XRPD = X-ray powder diffraction, sc-XRD = single-crystal X-ray diffraction. Ω is the unit cell volume, I is the interlayer distance between two As_2S_3 units. [a] Present work. [b] Mullen and Nowacki.[26]

one by about 4% (B3LYP-D3) and 8% (HSE06-D3). This effect is due to a combination of the shrinking of the b- and c-axes (*ca.* 2.5–4.3%), and a slight expansion of the a-axis. The theoretical

Fig. 3 Environmental scanning electron microscopy (ESEM) images at different magnifications of the sample of orpiment after scotch-tape cleavage. (a) General overview of the As_2S_3 multi-layer flake. (b) Example of a flat area with small fragments with a pseudo-hexagonal morphology. (c) Region characterized by multi-layered flakes forming ribbon-like structures. (d) Higher magnification of the stratification between the As_2S_3 layers. The images were obtained using an acceleration voltage of 15 kV and a water vapour pressure of 70 Pa.

Table 3 Fractional coordinates of the symmetrically inequivalent atoms in the orpiment As_2S_3 unit cell

Atom		B3LYP-D3[a]	HSE06-D3[a]	XRPD[a]	sc-XRD[b]
As1	x	0.2645	0.2640	0.2652(8)	0.2647
	y	0.1868	0.1874	0.1907(4)	0.1917
	z	0.8734	0.8725	0.8534(23)	0.8627
As2	x	0.4884	0.4892	0.4875(6)	0.4868
	y	0.3218	0.3225	0.3200(4)	0.3212
	z	0.3735	0.3733	0.3660(21)	0.3607
S1	x	0.3998	0.3995	0.4035(14)	0.4015
	y	0.1129	0.1132	0.1206(11)	0.1213
	z	0.5101	0.5041	0.5112(36)	0.5081
S2	x	0.3486	0.3490	0.3501(13)	0.3474
	y	0.4025	0.4039	0.3952(12)	0.3972
	z	0.0152	0.0089	0.0149(41)	0.0101
S3	x	0.1231	0.1226	0.1185(17)	0.1223
	y	0.2952	0.2968	0.2995(7)	0.2935
	z	0.5552	0.5512	0.5524(38)	0.5590

XRPD = X-ray powder diffraction, sc-XRD = single-crystal X-ray diffraction.[a] Present work. [b] Mullen and Nowacki.[26]

volume shrinking is then due to (i) the absence of thermal contributions to the lattice geometry, (ii) the use of hybrid functionals that generally provide a better description of the atomic bonds (*vide infra*) and (iii) the DFT-D3 correction. The variation observed in the *c* lattice parameter was reflected in the internal geometry, with As–S bonds slightly larger than the experimental ones up to about 1.5% and smaller S–As–S angles, especially the S2–As1–S3 and the S1–As2–S2 that are oriented along the *c*-axis. Conversely, the main reason for the smaller *b* lattice parameter is the calculated interlayer distance *I*, which was underestimated by about 8% with both DFT functionals. Indeed, the separation between the As_2S_3 layers was affected by the long-range interactions, with the DFT-D3 scheme probably providing an overestimation of the attraction between the layers. Despite these small differences, both theoretical approaches were able to provide a good description of the orpiment unit cell, considering also the different temperatures of the refinement, 0 K within DFT, and 298 K during the experiments.

In addition, to better highlight the importance of including the effects of long-range interactions in the physical treatment of van der Waals materials like orpiment, the lattice and internal geometry of the mineral were optimised without the DFT-D3 correction. The unit cell volume was severely overestimated by about 40% and 25% with the B3LYP and HSE06 functionals, respectively. This is mostly due to the increased length of the *b*-axis (+23% with B3LYP and +15% with HSE06) and *c*-axis (+20% and +11%), although the *a* lattice parameter was underestimated by about −3% with B3LYP and −1% with HSE06. While a rather large increase of the unit cell parameter *b* was expected, it is hypothesised that the overestimation of the *c*-axis length is probably due to a reduced intra-layer interaction between the lone pairs of the As and S atoms.

Vibrational features of bulk orpiment

As explained in the Introduction section, Raman spectroscopy is one of the main diagnostic tools used in mineralogy and archaeometry to characterise mineralogical species in a rock or artistic work. In the following, a detailed vibrational analysis of orpiment is reported.

The unit cell of the mineral contains four asymmetric units As_2S_3, for a total of $N = 20$ atoms. Thus, according to the character table of the $P2_1/n$ space group (C_{2h} point group), the total representation of the degrees of freedom of orpiment is given by:

$$\Gamma_{total} = 15A_g + 15A_u + 15B_g + 15B_u, \quad (17)$$

where *A* and *B* modes are non-degenerate modes that are symmetric and antisymmetric, respectively, to a rotation about the principal axis of the mineral. The subscripts "g (*gerade*)" and "u (*ungerade*)" express the symmetry or antisymmetry to the inversion centre, respectively. Furthermore, this symmetry element makes the *gerade* modes

active only in Raman spectroscopy, whereas the *ungerade* ones are IR-active. Of all the degrees of freedom, $\Gamma_{acoustic} = A_u + 2B_u$, *i.e.*, three modes are related to translations of the whole cell along the three crystallographic axes. The remaining 57 modes, *i.e.*,

$$\Gamma_{optic} = 15A_g + 14A_u + 15B_g + 13B_u \quad (18)$$

are associated with vibrational motions, with 30 modes expected in the Raman spectrum, whereas only 27 modes would be present in the infrared one.

Examples of the experimental analyses performed with confocal Raman microspectrometry on flat terraces of orpiment are shown in Fig. 4, which reports the area under investigation as seen with optical microscopy and the associated Raman spectra collected in different points marked with crosses in the image. All the spectra were collected using an excitation wavelength of 532 nm (green laser) with low-power settings to prevent any damage to the sample.

A similar analysis was performed on smaller flakes (thin layers) extracted from the orpiment specimen and deposited on aluminium stubs, with Fig. 5 showing some of these thin samples as an example. In this case, the green laser source was too energetic even for low output powers, hence a red laser (785 nm) was used (see Fig. 5d). No operations were performed on the reported Raman spectra but the removal of
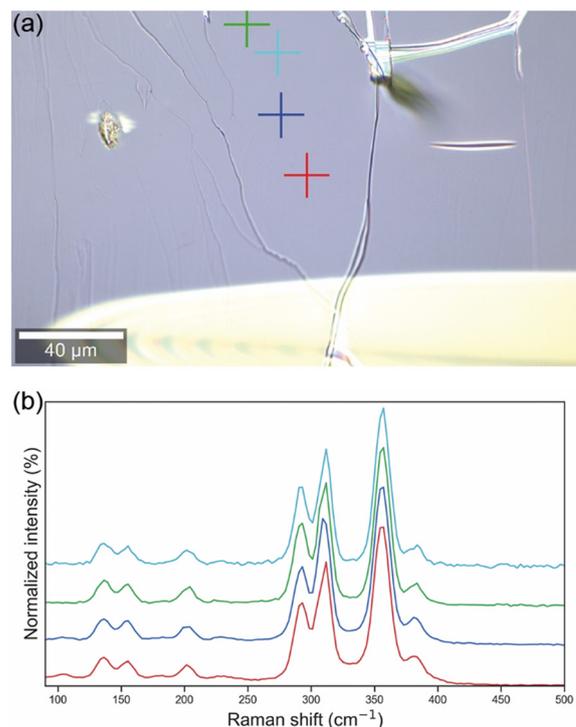
Fig. 4 Confocal Raman microspectrometry analysis of an atomic-flat terrace of orpiment As_2S_3. (a) Optical microscopy image of the area investigated. (b) Raman spectra (excitation wavelength λ = 532 nm) collected in the points marked with crosses in panel (a). The colours of the spectra match those of the markers in the optical image.

cosmic ray radiation and intensity normalization, the latter to ease the comparison between different acquisitions.

In general, the spectra presented sharp bands (mean full width at half maximum, FWHM, of about 10 cm^{-1}) that can be subdivided into two main regions: the first one was located between 250 cm^{-1} and 400 cm^{-1} and presented the most intense Raman bands, where four signals at about 292 cm^{-1}, 311 cm^{-1}, 356 cm^{-1} and 380 cm^{-1} can be observed. Conversely, the second spectral region was in the 100–250 cm^{-1} range, with four bands of weak intensity centred at 67 cm^{-1}, 137 cm^{-1}, 156 cm^{-1} and 203 cm^{-1}. In addition, it was observed with the 785 nm laser source a low-intensity, broad Raman band at about 180 cm^{-1}. This band could be due to an overlap of two vibrational modes at 179 cm^{-1} and 184 cm^{-1}, according to the deconvolution performed by using two Lorentzian peak functions.

The calculated Raman spectrum of orpiment (see Fig. S2 in the ESI†), the graphical inspection of the vibrational motions and the analysis of the potential energy distribution obtained from CRYSTAL simulations were employed to assign each mode to specific bands in the experimental spectra. A detailed comparison between the theoretical and experimental results is reported in Table 4.

The quantum mechanical approach was able to describe the overall features of the Raman spectrum of the mineral, with generally small shifts of the band positions and comparable intensities of the signals. However, the HSE06-D3 method proved to be slightly overbinding, with blue-shifted modes compared to the B3LYP-D3 approach. For this reason, the following presentation and comparison with the experiments were performed considering this latter functional.

According to the simulations, the most intense Raman signals were due to As–S out-of-plane stretching modes at 357 cm^{-1} (As1–S3 + As2–S3), 359 cm^{-1} (As1–S1 + As2–S1),

Table 4 Position and intensity (normalized to 1000) of the calculated and measured Raman bands, subdivided into the irreducible representations (IRREP) A_g and B_g

| IRREP | B3LYP-D3 | | $\Delta_{HSE06-D3}$ | Experimental | |
	v (cm^{-1})	I (‰)	v (cm^{-1})	532 nm	785 nm
A_g	33.7	103.6	0.7		
	42.8	33.8	0.1		
	69.7	5.2	0.9		
	80.5	79.8	0.4	67	68
	145.7	254.0	3.2	137	135
	157.1	65.4	1.8	154	154
	172.3	172.0	1.1		179
	192.6	50.9	2.0		
	210.1	320.4	0.0	202	201
	284.3	482.3	13.6	292	291
	314.0	597.6	9.9	311	310
	356.9	1000.0	10.5	356	355
	359.4	780.4	10.6		
	363.9	460.5	9.7		
	388.1	506.0	12.8	378	381
B_g	66.3	25.7	0.7	63	62
	84.3	6.6	−3.4		
	104.7	11.6	1.5		
	109.6	46.2	2.2		
	145.2	2.7	1.4		
	152.5	25.0	3.4		
	166.0	73.4	1.2		
	187.0	117.8	1.7	184	184
	199.5	31.1	4.9		
	310.5	211.4	9.3	307	308
	321.1	26.2	10.9		
	343.0	8.5	10.7		
	365.0	1.9	11.7		
	374.1	53.7	13.0		
	403.8	1.3	12.0		

HSE06-D3 was reported as differences with the B3LYP-D3 results ($\Delta_{HSE06-D3}$). Experimental Raman bands were reported according to the employed excitation laser source.

364 cm^{-1} (As2–S2) and 388 cm^{-1} (As1 – S2), and to As–S in-plane stretching modes at 314 cm^{-1} (As1–S1 + As2–S2), 311 cm^{-1} (As1–S1 + As2–S3) and 284 cm^{-1} (As1–S3). Thus, the theoretical results suggested that the experimental band at 355 cm^{-1} was given by two overlapping modes. Also, the shoulder calculated at 364 cm^{-1} was probably not detected at the experimental level because the spectral resolution of the instrument (2.7 cm^{-1}) was not able to discern this mode from the band centred at 356 cm^{-1}, resulting in a further convolution of the signals. For the sake of completeness, a graphical representation of the eigenvectors of atomic displacements is reported in Fig. S3 in the ESI.†

In the low-frequency region, i.e., below 100 cm^{-1}, the calculated modes were mostly rotations of the As_2S_3 units because of variations in the torsional angles. Here, the most intense signal was at ca. 80 cm^{-1}. The spectral region between 100 cm^{-1} and 250 cm^{-1} presented four low-intensity modes at 146 cm^{-1}, 172 cm^{-1}, 187 cm^{-1}, and 210 cm^{-1}, which were associated with in-plane, out-of-plane, symmetric and asymmetric As1–S–As2 bending modes, respectively. The modes at 146 cm^{-1}, 172 cm^{-1}, and 210 cm^{-1} correlated well
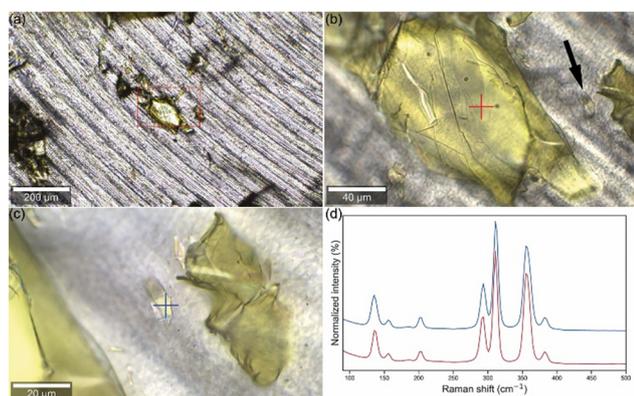
Fig. 5 Exfoliated orpiment analysed using confocal Raman microspectrometry. (a) Examples of the sherds that were analysed using confocal Raman microspectrometry. (b) Magnification of the area marked with the red rectangle in panel (a). (c) Magnification of the small orpiment fragment highlighted with the black arrow in panel (b). (d) Raman spectra (excitation wavelength λ = 785 nm) collected in the points marked with the red and blue crosses in panels (b) and (c), respectively. The colours of the spectra match those of the marks.

with those experimentally found at about 137 cm^{-1}, 154 cm^{-1} and 202 cm^{-1}, respectively.

DFT simulations were also used to calculate the infrared spectrum of the mineral, which is reported in Fig. S4 in the ESI.† Although IR spectroscopy was generally not employed in previous studies for the characterisation of chalcogenides, *e.g.*, in pigments, because of the lower limit of about 400 cm^{-1}, newer technologies such as nano-IR extended the detection capabilities to the low-wavenumber region. Thus, for the sake of completeness, the analysis of the vibrational modes active in infrared is here presented. As per the simulations, the most prominent IR bands of orpiment were in the range of 250–400 cm^{-1}, with the highest intensity signal at 282 cm^{-1} associated with the in-plane As1–S3 stretching mode, followed by the other As–S stretching modes at 314 cm^{-1} (in-plane), 356 cm^{-1} (out-of-plane), and 390 cm^{-1} (out-of-plane). In the As–S–As bending region, *i.e.*, 150–230 cm^{-1}, the highest bands were located at 185 cm^{-1} and about 150 cm^{-1}.

In addition, the phonon dispersion relations calculated on the 2 × 2 × 2 supercell containing 160 atoms with the DFT/B3LYP-D3 approach in the *Γ–Z–D–B–Γ–A–E–Z–C$_2$–Y$_2$–Γ* path in reciprocal space and the associated phonon density of states (PDOS) are reported in Fig. 6a. The separation between the phonon bands related to the stretching modes and those of the acoustic, rotational and bending modes is clearly visible and in agreement with the zone-centre Raman spectrum. The PDOS highlighted the higher contribution of sulphur atoms in the stretching of the As–S atoms, whereas the other modes showed a more uniform distribution between the two types of atoms. In addition, no negative phonon band, *i.e.*, the so-called soft phonons, was observed in the band structure, which means that the mineral is stable, further confirming the quality of the simulation approach employed to investigate orpiment.

Electronic properties

The band structure and the orbital-projected density of states (DOSS) of the mineral were calculated at the DFT/HSE06-D3 level to evaluate the electronic properties of orpiment As$_2$S$_3$. This hybrid functional generally provides better description of these properties because of more balanced short- and long-range electronic correlation effects than B3LYP. The same path in the first Brillouin zone previously described for the phonon band structure was used to sample the energy of the crystalline orbitals in reciprocal space. The use of the range-separated hybrid functional was justified by the accuracy for this kind of property, which is generally higher than that of other functionals.

According to the results reported in Fig. 6b, orpiment is a semi-conducting mineral with an indirect band gap E_g = 2.44 eV in the *Γ–A* direction. It is worth highlighting that the bands close to the Fermi level, both in the valence and in the conduction regions, showed small corrugation, meaning that direct electronic transitions, *i.e.*, optical transitions, may occur as well. For instance, the *Γ–Γ*
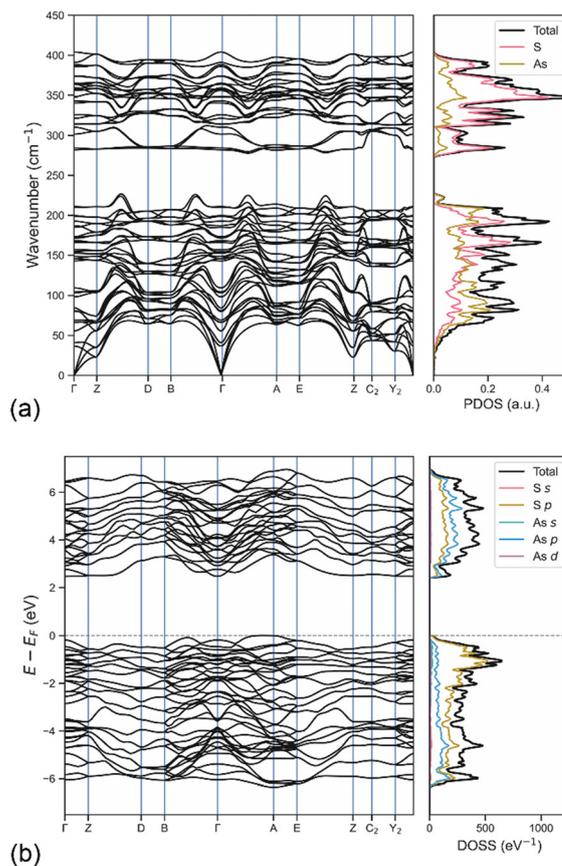

Fig. 6 Phonon and electronic properties of orpiment. (a) Phonon band structure and phonon density of states (PDOS) of bulk As$_2$S$_3$ calculated at the DFT/B3LYP-D3 level of theory. (b) Electronic band structure and density of states (DOSS) of bulk orpiment As$_2$S$_3$ obtained from DFT/HSE06-D3 simulations.

transition was observed at 2.63 eV and it could be useful for optoelectronic applications of the mineral. According to the projected DOSS, the highest valence bands were mainly given by S-3p states and by a small contribution arising from the As-4p and As-4s orbitals. In the conduction region, the bands are formed by hybridisation of the S-3p and As-4p states, with a slightly higher contribution from arsenic. Conversely, the As-3d orbitals lowly participated in the topmost valence and bottommost conduction bands. For the sake of completeness, similar electronic results were obtained at the DFT/B3LYP-D3 level of theory, albeit the calculated band gap was slightly larger (E_g = 2.87 eV) than that observed with the HSE06-D3 approach (E_g = 2.44 eV).

In addition, using the coupled-perturbed Kohn–Sham approach[56] described in the Computational methods section, it was possible to calculate the high-frequency dielectric tensor ε_∞, whose components were $\varepsilon_{\infty,xx}$ = 8.265, $\varepsilon_{\infty,yy}$ = 5.300 and $\varepsilon_{\infty,zz}$ = 6.505. By using the oscillator strength $f_{n,ij}$ of each calculated vibrational mode,[70] the static dielectric tensor components were calculated as $\varepsilon_{0,ij} = \varepsilon_{\infty,ij} + F_{ij}$, with $F_{ij} = \sum_n f_{n,ij}$, resulting in $\varepsilon_{0,xx}$ = 13.239, $\varepsilon_{0,yy}$ = 5.888 and $\varepsilon_{0,zz}$ = 9.956.

Elastic properties

Voigt's representation (6 × 6 matrix) of the stiffness tensor **C** of orpiment As_2S_3 (monoclinic system) is as follows:

$$\mathbf{C} = \begin{pmatrix} C_{11} & C_{12} & C_{13} & 0 & C_{15} & 0 \\ C_{12} & C_{22} & C_{23} & 0 & C_{25} & 0 \\ C_{13} & C_{23} & C_{33} & 0 & C_{35} & 0 \\ 0 & 0 & 0 & C_{44} & 0 & C_{46} \\ C_{15} & C_{25} & C_{35} & 0 & C_{55} & 0 \\ 0 & 0 & 0 & C_{46} & 0 & C_{66} \end{pmatrix}, \quad (19)$$

with 13 symmetry-independent elastic moduli. The calculation of the stiffness tensor was performed by aligning the crystallographic axes b and c parallel to the y and z Cartesian axes, respectively. The results obtained at the theoretical level using the B3LYP-D3 approach are reported in Table 5, alongside previously available results for comparison.

The mineral is highly anisotropic, with $C_{11} \gg C_{22} > C_{33}$, meaning that the uniaxial compression of the a-axis is more difficult than that of the other two crystallographic directions. In addition, it can be noted that the C_{15}, C_{25}, C_{35} and C_{46} moduli presented very small values, suggesting that the elastic properties of orpiment were closer to those of an orthorhombic crystal than those of a monoclinic one. This behaviour is consistent with the crystal structure of the mineral, whose β lattice parameter (90.46°) is close to the ideal 90°.

From the stiffness tensor, it is possible to calculate the elastic properties of polycrystalline aggregates, e.g., the bulk (K) and shear (μ) moduli according to Reuss (R, lower bound) and Voigt (V, upper bound) given by the following equations:[64]

$$K_V = (a + 2b)/9 \quad (20)$$

$$K_R = (d + 2e)^{-1} \quad (21)$$

$$\mu_V = (a + 3c - b)/15 \quad (22)$$

$$\mu_R = 15/[4(d - e) + 3f] \quad (23)$$

where

$$a = C_{11} + C_{22} + C_{33}, \; b = C_{12} + C_{13} + C_{23}$$
$$c = C_{44} + C_{55} + C_{66}, \; d = S_{11} + S_{22} + S_{33}$$
$$e = S_{12} + S_{13} + S_{23}, f = S_{44} + S_{55} + S_{66} \quad (24)$$

and $[S] = [C]^{-1}$ represents the compliance tensor, i.e., the inverse of the stiffness tensor.

The mean bulk and shear moduli are given by the Voigt–Reuss–Hill averaging method:[71]

$$K_{VRH} = \frac{K_V + K_R}{2} \quad (25)$$

$$\mu_{VRH} = \frac{\mu_V + \mu_R}{2} \quad (26)$$

with K_{VRH} and μ_{VRH} being the Voigt–Reuss–Hill averages of the bulk and shear moduli, respectively. The Young's modulus E and the Poisson's ratio v can also be calculated from the bulk and shear moduli using the following formulas:

$$E = \frac{9K\mu}{3K + \mu} \quad (27)$$

$$v = \frac{3K - 2\mu}{2(3K + \mu)} \quad (28)$$

In the present work, K_R = 23.9 GPa, K_V = 33.0 GPa, and K_{VRH} = 28.5 GPa; μ_R = 15.8 GPa, μ_V = 22.5 GPa, and μ_{VRH} = 19.2 GPa; E_R = 38.8 GPa, E_V = 55.0 GPa, and E_{VRH} = 46.9 GPa; and v_R = 0.229, v_V = 0.222, and v_{VRH} = 0.225.

Also, the same elastic properties were calculated for single crystals, which depend on the specific crystallographic direction.[72] Graphical representations of Young's modulus E, linear compressibility $\beta = 1/K$, shear modulus μ and Poisson's ratio v are reported in Fig. S5 in the ESI.† From the plots on the (xy), (xz), and (yz) Cartesian planes, the anisotropy of the elastic properties of orpiment was further highlighted.

Finally, the solution of the Christoffel equation[73] allowed the analysis of the propagation of acoustic (seismic) waves in orpiment. This eigenvalue equation led to three solutions, i.e., the slow secondary (v_{S2}), fast secondary (v_{S1}) and primary (v_P) wave velocities that were plotted as a Lambert projection of the upper hemisphere in Fig. S6a–c (ESI†). The results showed that the maximum acoustic velocity was along the [100] direction for v_P and v_{S1}. The percentages of anisotropy for v_P, v_{S1} and v_{S2} were 63.7%, 33.8 and 55.1, respectively, calculated as $A = 200(v_{max} - v_{min})/(v_{max} + v_{min})$. The S-wave anisotropy, which is also called shear wave splitting, is about 68%.

Discussion and conclusions

As previously explained in the Introduction section, the present work aimed to provide new, solid information on the

Table 5 Elastic moduli of orpiment (As_2S_3, space group $P2_1/n$)

Modulus (GPa)	B3LYP-D3[a]	Experimental[b]
C_{11}	118.8	99.6
C_{12}	15.2	—
C_{13}	25.5	20.6
C_{15}	0.1	−0.3
C_{22}	46.9	27.1
C_{23}	5.8	—
C_{25}	−1.5	—
C_{33}	38.4	21.9
C_{35}	1.0	−1.2
C_{44}	8.0	1.1
C_{46}	−2.6	0.2
C_{55}	34.0	24.0
C_{66}	17.9	0.7

[a] Present work. [b] Experimental Brillouin scattering measurements.[18]

crystallographic, lattice dynamics (*i.e.*, vibrational), electronic and elastic properties of crystalline orpiment As_2S_3, an important chalcogenide material that could be used in several technological applications.

The powdered specimen analysed by X-ray powder diffraction presented lattice parameters and atomic coordinates obtained from Rietveld structural refinement that were in good agreement with the single-crystal XRD diffraction results of Mullen and Nowacki,[74] with absolute variations in the range of 0.08–0.43% (see Table 1). The exfoliation of the orpiment sample for the subsequent ESEM-EDS and confocal Raman microspectrometry was carried out easily, suggesting and confirming the weak adhesion between the layers. The morphology from ESEM revealed that the cleaved sub-samples were multilayered As_2S_3 units; however, by employing suitable materials (*e.g.*, thermal release tapes) and substrates (SiO_2/Si wafers), this procedure could be enhanced to reach the desired two-dimensional single layer of orpiment.[75] Other cleaving techniques, such as liquid exfoliation,[76] are currently under investigation.

The collected Raman spectra of the mineral with both excitation sources of 532 nm and 785 nm were in good agreement with previous measurements reported in the scientific literature,[14,77,78] and the present new data could be used as references for future studies in archaeometry, archaeology and cultural heritage. The cross-correlation between experiments and DFT simulations helped in identifying which mode(s) belong to each visible band in the spectra and provided further information on the overlap of the peaks. In particular, in the work of Scheuermann and Ritter[14] three bands at 350.9 cm^{-1}, 353.5 cm^{-1} and 363.1 cm^{-1} were detected by using a high-resolution spectrometer (1 cm^{-1}). In the present work, these three bands were calculated from the DFT simulations at 357 cm^{-1} (shift of +7 cm^{-1}), 359 cm^{-1} (+6 cm^{-1}) and 364 cm^{-1} (+1 cm^{-1}), with intensities comparable to the experimental ones of Scheuermann and Ritter.[14] It is worth noting that the present Raman microspectrometry analysis detected only a single band centred at 356 cm^{-1} due to a combination of the lower resolution of the instrumentation (2.7 cm^{-1}) and the different intensities of the vibrational modes. Furthermore, Scheuermann and Ritter[14] observed a very weak band at 324 cm^{-1}, which was assigned to an overtone of the mode falling at 161 cm^{-1}, nevertheless, a fundamental vibrational mode (As–S stretching) was calculated in the present study at 321 cm^{-1}. Given the very small shift (*ca.* −3 cm^{-1}) and similar relative intensity of the bands, and since overtones fall below *nv* ($n = 2$ and *v* is the vibrational frequency), it is here suggested that the previous assignment was not properly defined.

The good comparison between the theoretical data and the experimental ones gave more confidence in evaluating other properties of bulk orpiment from DFT simulations. The indirect band gaps of As_2S_3 calculated at the HSE06-D3 and B3LYP-D3 levels of theory were 2.44 eV and 2.87 eV, respectively, which were in line with E_g = 2.6–2.7 eV

determined experimentally from the optical-absorption edge on crystalline samples.[79,80] These band gaps are larger than those of As_2S_3 glass[9,81–84] and biologically synthesised nanofibers,[85] both presenting an amorphous structure, whose E_g figures are about 2.1–2.5 eV. However, it must be remembered that the optical-absorption edge method provides direct valence–conduction band transitions, which for indirect-gap minerals and materials are larger. From this perspective, the *Γ–Γ* transition obtained from the HSE06-D3 approach (2.63 eV) was inside the E_g range measured during experiments.

Furthermore, the present study showed a slightly larger band gap compared to previous *ab initio* theoretical simulations, mainly because of the use of hybrid functionals. Generally, local density approximation (LDA) and generalized gradient approximation approaches led to underestimated E_g values, which is a well-documented issue in the scientific literature. For instance, Kaur and colleagues[86] obtained from DFT/GGA simulations with norm-conserving pseudopotentials E_g = 1.925 eV, whereas Patel and collaborators[87] calculated with the PBE (GGA) functional and projector-augmented wave basis sets a band gap of 2.08 eV. Notwithstanding the different E_g values, our investigation confirmed the indirect band gap and the semiconducting nature of crystalline As_2S_3 and provided more accurate results on the electronic band structure of the mineral.[38,39]

Regarding the elasticity of orpiment, as reported in the Introduction section, few data are available in the scientific literature from both experimental and theoretical perspectives. Brillouin scattering analysis was performed by McNeil and Grimsditch[18] on two natural samples which allowed obtaining ten of the thirteen independent elastic moduli, whose values were C_{11} = 99.6(1.0) GPa, C_{22} = 27.1(3) GPa, C_{33} = 21.9(1.4) GPa, C_{44} = 1.1(2) GPa, C_{55} = 24.0(8) GPa, C_{66} = 0.7(2) GPa, C_{13} = 20.6(1.9) GPa, C_{15} = −0.3(8) GPa, C_{35} = −1.2(9) GPa, and $|C_{11}|$ = 0.2(2) GPa (see Table 5). In general, the present simulation results were in good agreement with the experimental ones, with a small overestimation (maximum deviation of +20 GPa for the C_{11} component) that was due to the use of Gaussian-type orbital basis sets. As previously explained,[88,89] the stiffer behaviour originated from the Pulay stress, *i.e.*, an effect associated with the incompleteness of atom-centred basis sets. More into detail, the Pulay stress occurs during the derivation of the basis sets for the atomic positions and results in a small increase of the elastic moduli.

We found in the literature only the theoretical study on the elastic properties of As_2S_3 that was reported by Jiang and coworkers,[90] who performed molecular mechanics simulations using the Dreiding force field. However, the cited authors employed a non-canonical space group setting for orpiment, *i.e.*, the orthorhombic space group *Pnma*, imposing all lattice angles to 90°. The relaxed crystal structure (*a* = 10.779 Å, *b* = 3.304 Å, *c* = 13.565 Å) exhibited relatively large variations and a different crystal orientation compared to the experimental XRD refinements. The modelling and

computational approach proposed by Jiang and coworkers[90] could explain the deviations observed in the calculated elastic moduli, *e.g.*, C_{11} = 31.3 GPa, C_{22} = 130.4 GPa, C_{33} = 32.9 GPa, and C_{44} = 7.9 GPa. Also, only seven of the nine independent elastic moduli for an orthorhombic system[91] were reported, and no information on the crystal orientation to the Cartesian axes during the calculation of the elastic tensor was provided. According to the space group employed by the authors, it was supposed that the crystallographic axes were oriented parallel to the ones of the Cartesian reference system, *i.e.*, $a||x$, $b||y$ and $c||z$. Instead, the present simulations at the DFT/B3LYP-D3 level of theory considered the correct crystallographic setting of the mineral, confirming the experimental results from Brillouin scattering and providing the complete set of thirteen independent elastic tensor components.

All the present data suggest that orpiment As_2S_3 (space group $P2_1/n$) is a potentially interesting mineral and material with peculiar structural, electronic and elastic properties that could be exploited in two-dimensional materials research and development of devices. The proposed combined experimental–theoretical approach with cross-correlation of the results provided new insights into this material and assessed the quality and predictive power of the simulations. This study suggested that crystalline As_2S_3 (i) is phononically and mechanically stable under ambient conditions, (ii) presents an indirect band gap of about 2.44 eV and an optical transition of *ca.* 2.63 eV, and (iii) can be easily exfoliated in thin, few-layer structures. Hence, the cleavage can be pushed down to the monolayer without extreme difficulties using the scotch tape technique.

The present research aimed at obtaining a fundamental understanding of the features of orpiment, which presents layers with a puckered morphology at the atomic scale. This peculiar feature distinguishes this mineral from other well-known 2D materials, for instance, graphene and monolayer molybdenite MoS_2, which instead exhibit atomic-flat surfaces. The atomic structure, *i.e.*, the crystallography, is one of the key properties that control both the interaction between two layered materials and the modulation of the physical (electronic, optical, elastic) properties of the interface. Work is in progress in this sense to exfoliate single monolayers of As_2S_3, whose mineralogical, physical and chemical properties will be investigated with the same cross-correlation approach here employed to understand how extreme exfoliation (*i.e.*, down to a single- and few-layers of As_2S_3) changes the behaviour of the material. Then, new applications of this two-dimensional material could be devised in different applications, for example, optoelectronics, 2D materials development, sensors and catalysis.

Data availability

The results obtained in the present work are also available in a data repository at **https://doi.org/10.17632/wnfzg8rgsz.1**.

Author contributions

Conflicts of interest

There are no conflicts to declare.

Acknowledgements

References

1 L. Yildiz, in *Comprehensive Energy Systems*, 2018, vol. 1–5, pp. 521–567.
2 L. E. Bell, *J. Electron. Mater.*, 2009, **38**, 1344–1349.
3 A. G. El-Shamy, *Mater. Today Phys.*, 2023, **35**, 101101.
4 M. L. Kolhe, K. J. Karande and S. G. Deshmukh, *Artificial Intelligence, Internet of Things (IoT) and Smart Materials for Energy Applications*, 2022.
5 L. Wang, L. Huang, W. C. Tan, X. Feng, L. Chen, X. Huang and K. W. Ang, *Small Methods*, 2018, **2**, 1700294.
6 P. You, G. Tang and F. Yan, *Mater. Today Energy*, 2019, **11**, 128–158.
7 B. J. Eggleton, B. Luther-Davies and K. Richardson, *Nat. Photonics*, 2011, **5**, 141–148.
8 P. Němec, J. Jedelský, M. Frumar, Z. Černošek and M. Vlček, *J. Non-Cryst. Solids*, 2005, **351**, 3497–3502.
9 I. Banik, *J. Optoelectron. Adv. Mater.*, 2016, **18**, 226–234.
10 P. Bonazzi and L. Bindi, *Z. Kristallogr.*, 2008, **223**, 132–147.
11 A. Patel, D. Singh, Y. Sonvane, P. B. Thakor and R. Ahuja, *Mater. Res. Proc.*, 2022, **22**, 57–64.
12 A. van Loon, P. Noble, A. Krekeler, G. Snickt, K. Janssens, Y. Abe, I. Nakai and J. Dik, *Heritage Sci.*, 2017, **5**, 22.
13 K. P. Smith and G. Ólafsson, *J. Archaeol. Sci. Rep.*, 2023, **47**, 103724.
14 W. Scheuermann and G. J. Ritter, *Z. Naturforsch., A: Phys. Sci.*, 1969, **24**, 408–411.
15 D. B. Jones, J. R. Gascooke and C. T. Gibson, *Carbon*, 2024, **229**, 119546.
16 D. Mrđenović, Z. F. Cai, Y. Pandey, G. L. Bartolomeo, R. Zenobi and N. Kumar, *Nanoscale*, 2022, **15**, 963–974.

17 S. Zhang, N. Zhang, Y. Zhao, T. Cheng, X. Li, R. Feng, H. Xu, Z. Liu, J. Zhang and L. Tong, *Chem. Soc. Rev.*, 2018, **47**, 3217–3240.

18 L. E. McNeil and M. Grimsditch, *Phys. Rev. B: Condens. Matter Mater. Phys.*, 1991, **44**, 4174–4177.

19 A. K. Geim and K. S. Novoselov, *Nat. Mater.*, 2007, **6**, 183–191.

20 N. Doebelin and R. Kleeberg, *J. Appl. Crystallogr.*, 2015, **48**, 1573–1580.

21 J. Bergmann and R. Kleeberg, *Mater. Sci. Forum*, 1998, **278-281**, 300–305.

22 R. Dovesi, A. Erba, R. Orlando, C. M. Zicovich-Wilson, B. Civalleri, L. Maschio, M. Rerat, S. Casassa, J. Baima, S. Salustro and B. Kirtman, *Wiley Interdisc. Rev.: Comput. Mol. Sci.*, 2018, **8**, E1360.

23 A. D. Becke, *J. Chem. Phys.*, 1993, **98**, 5648–5652.

24 C. T. Lee, W. T. Yang and R. G. Parr, *Phys. Rev. B: Condens. Matter Mater. Phys.*, 1988, **37**, 785–789.

25 J. Heyd, G. E. Scuseria and M. Ernzerhof, *J. Chem. Phys.*, 2003, **118**, 8207–8215.

26 D. J. E. Mullen and W. Nowacki, *Z. Kristallogr.*, 1972, **136**, 48–65.

27 J. P. Perdew, K. Burke and M. Ernzerhof, *Phys. Rev. Lett.*, 1996, **77**, 3865–3868.

28 G. Ulian and G. Valdrè, *J. Appl. Crystallogr.*, 2024, **57**, 220–231.

29 G. Ulian and G. Valdrè, *Minerals*, 2022, **12**, 1323.

30 F. Pascale, C. M. Zicovich-Wilson, F. L. Gejo, B. Civalleri, R. Orlando and R. Dovesi, *J. Comput. Chem.*, 2004, **25**, 888–897.

31 F. Pascale, S. Tosoni, C. Zicovich-Wilson, P. Ugliengo, R. Orlando and R. Dovesi, *Chem. Phys. Lett.*, 2004, **396**, 308–315.

32 G. Ulian, D. Moro and G. Valdrè, *Compos. Struct.*, 2021, **255**, 112978.

33 G. Ulian, D. Moro and G. Valdrè, *Am. Mineral.*, 2021, **106**, 1928–1939.

34 W. F. Perger, *Int. J. Quantum Chem.*, 2010, **110**, 1916–1922.

35 D. Moro, G. Ulian and G. Valdrè, *Appl. Clay Sci.*, 2019, **172**, 28–39.

36 D. Moro, G. Ulian and G. Valdrè, *J. Microsc.*, 2020, **280**, 204–221.

37 D. Moro, G. Ulian and G. Valdrè, *Appl. Clay Sci.*, 2020, **197**, 105777.

38 G. Ottonello, B. Civalleri, J. Ganguly, M. V. Zuccolini and Y. Noel, *Phys. Chem. Miner.*, 2009, **36**, 87–106.

39 G. Ulian, D. Moro and G. Valdrè, *Am. Mineral.*, 2020, **105**, 1212–1222.

40 G. Ulian and G. Valdrè, *Int. J. Quantum Chem.*, 2020, **120**, e26069.

41 S. Grimme, J. Antony, S. Ehrlich and H. Krieg, *J. Chem. Phys.*, 2010, **132**, 154104.

42 S. Grimme, *J. Comput. Chem.*, 2006, **27**, 1787–1799.

43 A. D. Becke and E. R. Johnson, *J. Chem. Phys.*, 2005, **123**, 154101.

44 E. R. Johnson and A. D. Becke, *J. Chem. Phys.*, 2005, **123**, 024101.

45 E. R. Johnson and A. D. Becke, *J. Chem. Phys.*, 2006, **124**, 174104.

46 G. Ulian and G. Valdrè, *Appl. Clay Sci.*, 2023, **246**, 107166.

47 G. Ulian and G. Valdrè, *Phys. Chem. Miner.*, 2019, **46**, 101–117.

48 G. Ulian and G. Valdrè, *Sci. Rep.*, 2023, **13**, 23090.

49 J. Heyd, J. E. Peralta, G. E. Scuseria and R. L. Martin, *J. Chem. Phys.*, 2005, **123**, 174101.

50 H. J. Monkhorst and J. D. Pack, *Phys. Rev. B: Solid State*, 1976, **8**, 5188–5192.

51 C. G. Broyden, *IMA J. Appl. Math.*, 1970, **6**, 222–231.

52 C. G. Broyden, *IMA J. Appl. Math.*, 1970, **6**, 76–90.

53 R. Fletcher, *Comput. J.*, 1970, **13**, 317–322.

54 D. Goldfarb, *Math. Comput.*, 1970, **24**, 23–26.

55 D. F. Shanno, *Math. Comput.*, 1970, **24**, 647–656.

56 A. M. Ferrari, L. Valenzano, A. Meyer, R. Orlando and R. Dovesi, *J. Phys. Chem. A*, 2009, **113**, 11289–11294.

57 G. Placzek, *Handbuch der Radiologie*, Akademische Verlagsgesellschaft, Leipzig, 1934.

58 L. Maschio, B. Kirtman, M. Rerat, R. Orlando and R. Dovesi, *J. Chem. Phys.*, 2013, **139**, 164101.

59 M. Ferrero, M. Rerat, B. Kirtman and R. Dovesi, *J. Chem. Phys.*, 2008, **129**, 244110.

60 M. Ferrero, M. Rerat, R. Orlando and R. Dovesi, *J. Comput. Chem.*, 2008, **29**, 1450–1459.

61 M. Ferrero, M. Rerat, R. Orlando and R. Dovesi, *J. Chem. Phys.*, 2008, **128**, 014110.

62 M. T. Dove, *Introduction to Lattice Dynamics*, Cambridge University Press, 1993.

63 W. F. Perger, J. Criswell, B. Civalleri and R. Dovesi, *Comput. Phys. Commun.*, 2009, **180**, 1753–1759.

64 J. F. Nye, *Physical properties of crystals*, Oxford University Press, Oxford, 1957.

65 A. Erba, *Phys. Chem. Chem. Phys.*, 2016, **18**, 13984–13992.

66 G. Ulian and G. Valdrè, *Acta Crystallogr., Sect. B: Struct. Sci., Cryst. Eng. Mater.*, 2019, **75**, 1042–1059.

67 J. W. Jaeken and S. Cottenier, *Comput. Phys. Commun.*, 2016, **207**, 445–451.

68 G. Ulian and G. Valdrè, *J. Appl. Crystallogr.*, 2022, **55**, 386–396.

69 G. Ulian and G. Valdrè, *Comput. Geosci.*, 2024, **188**, 105615.

70 G. Ulian and G. Valdrè, *Sci. Rep.*, 2023, **13**, 2725.

71 R. Hill, *Proc. Phys. Soc., London, Sect. A*, 1952, **65**, 349–354.

72 R. Gaillac, P. Pullumbi and F. X. Coudert, *J. Phys.: Condens. Matter*, 2016, **28**, 275201.

73 M. J. P. Musgrave, *Crystal Acoustics: introduction to the study of elastic waves and vibrations in crystals*, Holden-Day, San Francisco, CA, USA, 1970.

74 D. J. E. Mullen and W. Nowacki, *Z. Kristallogr., Kristallgeom., Kristallphys., Kristallchem.*, 1972, **136**, 48–65.

75 F. Bonaccorso, A. Lombardo, T. Hasan, Z. P. Sun, L. Colombo and A. C. Ferrari, *Mater. Today*, 2012, **15**, 564–589.

76 U. Khan, A. O'Neill, M. Lotya, S. De and J. N. Coleman, *Small*, 2010, **6**, 864–871.

77 F. S. Gard, D. M. Santos, M. B. Daizo, J. L. Mijares, P. B. Bozzano, C. A. Danón, M. Reinoso and E. B. Halac, *Surf. Interface Anal.*, 2020, **52**, 755–769.

78 R. Mazzeo, P. Baraldi, R. Lujàn and C. Fagnano, *J. Raman Spectrosc.*, 2004, **35**, 678–685.

79 J. M. Besson, J. Cernogora and R. Zallen, *Phys. Rev. B: Condens. Matter Mater. Phys.*, 1980, **22**, 3866–3876.

80 R. Zallen and D. F. Blossey, in *Optical and Electrical Properties*, ed. P. A. Lee, Springer Netherlands, Dordrecht, 1976, pp. 231–272, DOI: **10.1007/978-94-010-1478-6_3**.

81 P. E. Lippens, M. A. El Idrissi Raghni, J. Olivier-Fourcade and J. C. Jumas, *J. Alloys Compd.*, 2000, **298**, 47–50.

82 V. Matějec, J. Pedliková and I. Barton, *J. Sol-Gel Sci. Technol.*, 2018, **87**, 696–703.

83 V. Matějec, J. Pedliková, I. Barton, J. Zavadil and P. Kostka, *J. Non-Cryst. Solids*, 2016, **431**, 47–51.

84 M. Popescu and D. Mezzane, *Optoelectron. Adv. Mater., Rapid Commun.*, 2008, **2**, 26–28.

85 I. R. McFarlane, J. R. Lazzari-Dean and M. Y. El-Naggar, *Acta Biomater.*, 2015, **13**, 364–373.

86 V. Kaur, S. K. Tripathi and S. Prakash, *AIP Conf. Proc.*, 2016, **1728**, 020433.

87 A. Patel, D. Singh, Y. Sonvane, P. B. Thakor and R. Ahuja, *Comput. Mater. Sci.*, 2020, **183**, 109913.

88 G. Ulian, D. Moro and G. Valdrè, *Compos., Part C: Open Access*, 2021, **6**, 100184.

89 G. Ulian and G. Valdrè, *Sci. Rep.*, 2022, **12**, 299.

90 L. Jiang, M. Wu, P. Shi and C. Zhang, *Int. J. Photoenergy*, 2020, **2020**, 8852665.

91 F. Mouhat and F. X. Coudert, *Phys. Rev. B: Condens. Matter Mater. Phys.*, 2014, **90**, 224104.